

# A Fully Ab-Initio Spin-Lattice Dynamics Framework for Magnetic Materials

Xianxi Zhang,<sup>1</sup> Hongyu Yu,<sup>1</sup> Liangliang Hong,<sup>1</sup> and Hongjun Xiang<sup>1,\*</sup>

<sup>1</sup>*Key Laboratory of Computational Physical Sciences (Ministry of Education),  
Institute of Computational Physical Sciences, State Key Laboratory of Surface Physics,  
and Department of Physics, Fudan University, Shanghai 200433, China*

(Dated: May 5, 2026)

Coupled spin-lattice dynamics (SLD) underlie a wide range of magnetic phenomena, yet a unified first-principles framework that propagates both degrees of freedom without empirical parameterization has remained elusive. We present a fully *ab initio* SLD approach integrated into VASP, in which interatomic forces and effective magnetic fields are obtained at each time step from self-consistent constrained-moment density-functional calculations. The method is validated on four materials spanning ferromagnetic, non-collinear, and geometrically frustrated orders, recovering the correct magnetic ground state in every case from random initial conditions. SLD trajectories also provide physically correlated training data for magnetic machine-learning potentials, as demonstrated for BiFeO<sub>3</sub> by a reduction of up to approximately one order of magnitude in energy MAE over training on randomized spin configurations. This framework opens a practical first-principles route to finite-temperature spin-lattice coupled phenomena in magnetic materials.

## I. INTRODUCTION

The interplay between spin and lattice degrees of freedom plays a central role in a wide range of condensed-matter phenomena, including ultrafast demagnetization [1, 2], magnetostructural phase transitions [3], and magnon–phonon scattering [4, 5]. From a technological perspective, the development of spintronic devices [6, 7] and ultrafast magnetic recording [8, 9] has further underscored the need for a microscopic, finite-temperature description of the coupled evolution of spin and lattice degrees of freedom. At the microscopic level, this coupling has two prominent contributions: the dependence of magnetic exchange interactions  $J_{ij}$  on interatomic distances, and spin-orbit-mediated transfer of angular momentum between the magnetic and lattice subsystems. A comprehensive understanding of these phenomena therefore requires a theoretical description that treats lattice and spin degrees of freedom on an equal footing. While static first-principles calculations have successfully elucidated the ground-state properties of magnetic materials [10, 11], describing finite-temperature thermodynamics and nonequilibrium evolution necessitates a dynamical approach that explicitly accounts for the coupling between spins and the lattice.

Conventionally, spin dynamics and their coupling to the lattice are simulated by constructing model Hamiltonians with parametrized exchange couplings  $J_{ij}$  from first-principles calculations and propagating the spins via the Landau–Lifshitz–Gilbert (LLG) equation [12–17]. Although computationally efficient, these methods are limited by the fixed nature of the parametrized couplings, which cannot capture regimes where exchange interactions are strongly modulated by lattice distortions or where the electronic structure changes significantly from

the reference state used in the fitting. In contrast, standard *ab initio* molecular dynamics (AIMD) provides an accurate first-principles description of lattice dynamics, but it does not treat spin orientations as independent dynamical variables and therefore neglects the transverse spin fluctuations and precessional dynamics central to LLG evolution. Time-dependent density-functional theory can in principle provide a fully first-principles description of coupled electronic, spin, and lattice dynamics, but its computational cost currently limits its use for the length and time scales relevant to finite-temperature simulations in realistic materials [18, 19]. What remains lacking, therefore, is a practical first-principles framework in which the effective magnetic fields are obtained directly from DFT at each time step, eliminating the intermediate mapping onto parametrized exchange interactions.

In this work, we present a fully *ab initio* SLD method seamlessly integrated into the Vienna *Ab initio* Simulation Package (VASP) [20, 21]. Our approach couples the Newtonian equations of motion for the lattice with the stochastic LLG equation for the magnetic moments. Crucially, both the interatomic forces and the effective magnetic fields that drive the spin dynamics are obtained self-consistently at every time step from constrained local-moment DFT calculations, without requiring an intermediate mapping onto parametrized exchange interactions [22]. This framework therefore enables the simultaneous evolution of atomic and spin degrees of freedom on the same first-principles footing, allowing the dynamic coupling and energy exchange between the lattice and spin subsystems to be captured directly. We validate the implementation across four representative systems spanning distinct electronic and magnetic regimes—a two-dimensional semiconductor (CrI<sub>3</sub>), an itinerant ferromagnet (bcc Fe), a correlated 5*d* oxide (Cd<sub>2</sub>Os<sub>2</sub>O<sub>7</sub>), and a geometrically frustrated spinel (MgCr<sub>2</sub>O<sub>4</sub>)—and find that, in all four cases, the simulations evolve from random initial conditions to the correct magnetic ground

\* [hxiang@fudan.edu.cn](mailto:hxiang@fudan.edu.cn)

state without ad hoc parameter adjustments.

Beyond enabling direct spin-lattice simulations, the present *ab initio* SLD framework also provides a route to generating training data for spin-aware machine-learning models. Direct first-principles SLD nevertheless remains computationally demanding for larger supercells, longer trajectories, and the extensive sampling needed for finite-temperature studies. In this context, spin-aware machine-learning models provide a natural way to extend spin-lattice simulations to larger scales, but their performance depends critically on the distribution and quality of the training data. In non-magnetic systems, practical strategies for constructing training distributions tailored to the target thermodynamic or dynamical regime are already well developed [23–26], whereas for magnetic systems the choice of a suitable distribution in the combined space of atomic and spin degrees of freedom is less straightforward. A common baseline is to combine structural snapshots with independently randomized magnetic configurations, but this construction does not preserve the correlations between local lattice distortions and spin configurations, whereas SLD trajectories retain these correlations because atomic positions and magnetic moments co-evolve under forces and effective fields obtained from the same first-principles calculations. This motivates a controlled benchmark for an 80-atom BiFeO<sub>3</sub> supercell, in which we compare SpinGNN, a spin-aware graph neural network model, trained on SLD-derived data with the same model trained on a reference dataset constructed from the same initial structures but paired with randomized magnetic configurations. Our goal is not to claim the universal superiority of SLD-derived data, but to test whether they offer an advantage for the physically relevant spin-lattice configurations encountered in subsequent dynamical simulations.

## II. METHODOLOGY AND IMPLEMENTATION

### A. Theoretical Framework

The present formulation employs two approximations commonly adopted in first-principles spin-dynamics studies. The first is the *spin-adiabatic approximation*, which assumes that the orientations of local magnetic moments vary on a much slower time scale than their magnitudes, so that the moment magnitudes adapt instantaneously to the local environment and do not require their own equations of motion, with the orientations being treated as classical dynamical variables [12]. The second is the *atomic-moment approximation*, under which each atomic site  $i$  carries a local magnetic moment  $\mathbf{M}_i$ , defined as the spatial integral of the spin-density distribution in the region surrounding atom  $i$  [27].

Within these approximations, the coupled spin-lattice dynamics are governed by the classical equations of motion for the ions and the stochastic Landau-Lifshitz-

Gilbert (LLG) equation for the spins:

$$m_i \ddot{\mathbf{R}}_i = \mathbf{F}_i, \quad (1)$$

$$\begin{aligned} \frac{d\mathbf{M}_i}{dt} = & -\gamma \mathbf{M}_i \times (\mathbf{B}_i + \mathbf{b}_i) \\ & - \frac{\alpha}{|\mathbf{M}_i|} \mathbf{M}_i \times [\mathbf{M}_i \times (\mathbf{B}_i + \mathbf{b}_i)]. \end{aligned} \quad (2)$$

Here  $m_i$  and  $\mathbf{R}_i$  denote the mass and position of atom  $i$ , and  $\mathbf{F}_i$  is the force acting on that atom.  $\mathbf{M}_i$  represents the local magnetic moment on site  $i$ ,  $\mathbf{B}_i$  is the effective magnetic field conjugate to it, and  $\mathbf{b}_i$  is a stochastic field representing thermal fluctuations in the spin subsystem. The constants  $\gamma$  and  $\alpha$  are the gyromagnetic ratio and Gilbert damping parameter, respectively.

To evaluate the effective magnetic field  $\mathbf{B}_i$  required by the LLG equation, we employ VASP’s built-in constrained local-moment approach [22]. In this scheme, a penalty term is added to the Kohn-Sham energy functional to constrain the orientation of each local moment  $\mathbf{M}_i$  towards a prescribed direction  $\hat{\mathbf{e}}_i^0$ :

$$E_p = \lambda \sum_i [\mathbf{M}_i - \hat{\mathbf{e}}_i^0 (\hat{\mathbf{e}}_i^0 \cdot \mathbf{M}_i)]^2, \quad (3)$$

Here  $\lambda$  is a penalty strength parameter that enforces the constraint; in the limit  $\lambda \rightarrow \infty$  the moment orientation  $\mathbf{M}_i$  coincides exactly with  $\hat{\mathbf{e}}_i^0$ . The functional derivative of the penalty term with respect to the spin density yields a constraining magnetic field,

$$\mathbf{B}_i^{\text{con}} = \frac{2\lambda}{M_i} [\mathbf{M}_i - \hat{\mathbf{e}}_i^0 (\hat{\mathbf{e}}_i^0 \cdot \mathbf{M}_i)], \quad (4)$$

which by construction lies nearly perpendicular to  $\mathbf{M}_i$ .

At self-consistency, the total energy  $E = E_{\text{KS}} + E_p$  is stationary with respect to the spin density, which directly implies  $\mathbf{B}_i^{\text{eff}} = -\mathbf{B}_i^{\text{con}}$ , i.e., the constraining field output by VASP equals the negative of the true effective field driving the spin dynamics [22, 28]. This identity has been established analytically by Brännvall et al. and holds for any exchange-correlation functional, independent of the mean-field structure of the Hamiltonian [28]. It has also been verified numerically via finite-difference calculations of the energy gradient with respect to moment rotation; see Ref. [29] and the Supplemental Material for independent confirmations. The effective field  $\mathbf{B}_i = -(1/M_i) \partial E_0 / \partial \theta_i$  is therefore directly available from the VASP output at each SLD step without any additional computation.

### B. Numerical Implementation

The ionic equations of motion (1) are integrated using the standard velocity-Verlet scheme [30] implemented in VASP, while the LLG equation (2) is integrated using the semi-implicit SIB algorithm of Mentink et al. [31], which conserves the spin length and is numerically stable.

Convergence tests with time steps ranging from 0.2 to 2 fs showed that the spin integration remained accurate up to 1 fs, whereas steps of  $\approx 2$  fs introduced noticeable numerical artifacts. Unless otherwise noted, a time step of 1 fs is adopted throughout this work.

The stochastic field  $\mathbf{b}_i$  in Eq. (2) is modeled as Gaussian white noise interpreted in the Stratonovich sense [31], with zero mean and correlations given by the fluctuation–dissipation theorem:

$$\langle b_i^\mu(t) b_j^\nu(t') \rangle = \frac{2\alpha k_B T}{(1 + \alpha^2) \gamma M_i} \delta_{ij} \delta_{\mu\nu} \delta(t - t'), \quad (5)$$

where  $\mu, \nu$  label Cartesian components and  $T$  is the temperature. This relation ensures that the spin subsystem samples the canonical equilibrium distribution at temperature  $T$  [31].

As illustrated in Fig. 1, at each time step a self-consistent constrained-moment DFT calculation yields the interatomic forces  $\{\mathbf{F}_i\}$  and the effective magnetic fields  $\{\mathbf{B}_i\}$ , which then advance the ionic positions via velocity-Verlet and the spin directions via the SIB integrator, respectively. The updated ionic positions and spin orientations then enter the next constrained-moment DFT calculation, with the latter defining the new constraint directions  $\hat{\mathbf{e}}_i^0$ , thereby closing the dynamical loop.

This formulation is implemented within VASP, allowing direct use of its native functionalities—including the projector-augmented-wave (PAW) method [32, 33], spin-orbit coupling, and external-field perturbations—for self-consistent spin-lattice dynamics simulations. New tags have been introduced into the VASP input file (INCAR) to control the SLD workflow, while the relevant output quantities are written to a dedicated file (ASDCAR), leaving the standard VASP output unchanged. Details of these input tags and the auxiliary analysis toolkit (sldkit) for post-processing and visualization are described in the Supplemental Material.

### III. VALIDATION VIA MAGNETIC GROUND-STATE REPRODUCTION

To validate the physical accuracy of the *ab initio* SLD approach, we examine its ability to reproduce the magnetic ground states of four representative materials with distinct electronic and magnetic characteristics. These materials are selected because their magnetic ground states are experimentally well established and because such magnetic orders cannot be stabilized by standard static DFT calculations without external constraints, thereby providing stringent benchmarks for the present approach. Unless otherwise specified, all SLD simulations were performed in the isothermal-isobaric ( $NpT$ ) ensemble using a Langevin thermostat and the Parrinello–Rahman barostat [34], so that atomic positions, lattice parameters, and magnetic moment orientations relax simultaneously within a unified dynamical framework. In all simulations, the Perdew–Burke

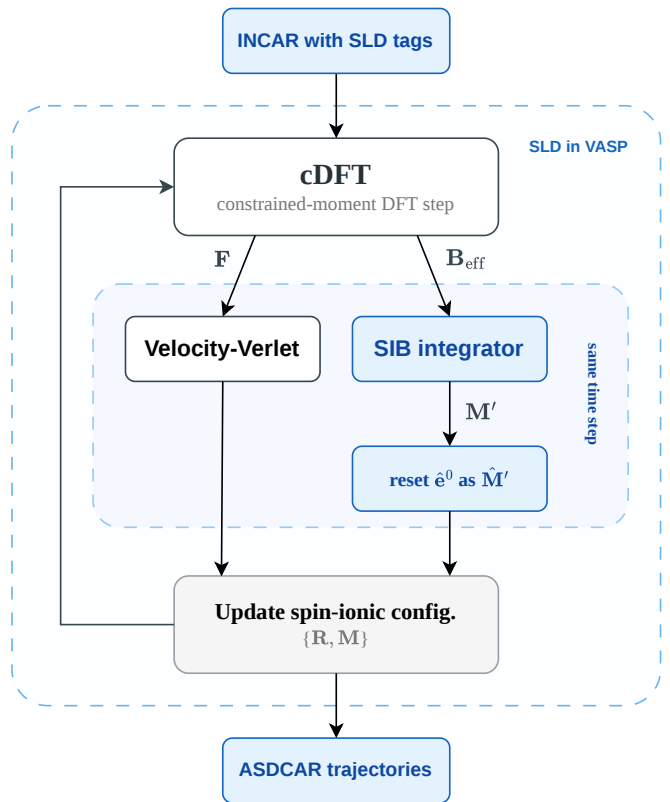


FIG. 1. Schematic of the *ab initio* SLD dynamical loop implemented in VASP. At each time step, a constrained-moment DFT calculation yields both the interatomic forces  $\{\mathbf{F}_i\}$  and the effective magnetic fields  $\{\mathbf{B}_i\}$ , which are used to advance ionic positions via velocity-Verlet and spin directions via the SIB integrator, respectively.

Ernzerhof (PBE) exchange-correlation functional [35] was employed. In addition, a relatively large Gilbert damping parameter was adopted solely to accelerate relaxation toward the magnetic ground state; tests with smaller values produce the same final configurations but require longer trajectories.

We first assess the method for two representative collinear ferromagnets, monolayer  $\text{CrI}_3$  and bcc Fe, which provide complementary tests in a two-dimensional local-moment magnet and a three-dimensional itinerant metal, respectively. Monolayer  $\text{CrI}_3$  is a prototypical two-dimensional van der Waals ferromagnet with an out-of-plane Ising easy axis [36]; the computational details are summarized in Table I. Starting from fully random spin orientations on the Cr sites, the simulation converges within 2 ps to the correct out-of-plane ferromagnetic ground state [Fig. 2(a)]. Bcc Fe, by contrast, is a canonical itinerant ferromagnet that still supports well-defined local moments, thereby providing a useful test of the present framework in a metallic system, with the corresponding simulation parameters also listed in Table I. When initialized from random moment orientations, the simulation at 300 K develops the expected collinear ferromagnetic order, with the magnetization fluctuating

around a finite value corresponding to an average moment of approximately  $2\mu_B$  per Fe atom [Fig. 2(b)]. These two cases confirm that the present framework reproduces collinear ferromagnetic order in both insulating and metallic systems.

$\text{Cd}_2\text{Os}_2\text{O}_7$  is a correlated  $5d$  oxide that exhibits a non-collinear all-in-all-out (AIAO) spin configuration, in which the Os moments on each tetrahedron either all point inward or all point outward [37]; computational details are given in Table I. Starting from random spin orientations on all Os sites, the simulation converges rapidly to the AIAO arrangement. To quantify the degree of ordering we employ the normalized AIAO order parameter [38, 39]

$$m_s^2 = \frac{4}{N^2} \sum_{a=1}^4 \left| \sum_i \mathbf{M}_i^a \right|^2, \quad (6)$$

where  $\mathbf{M}_i^a$  is the magnetic moment of the  $a$ -th Os in the  $i$ -th unit cell and  $N$  is the total number of Os atoms. The converged value  $m_s \approx 0.9$ , slightly below unity due to finite-size effects in the single conventional unit cell, confirms that the simulation reproduces the AIAO magnetic ground state [Fig. 2(c,d)].

To test the method in a system with strong geometric frustration, we simulate the spinel oxide  $\text{MgCr}_2\text{O}_4$  [40], in which the magnetic  $\text{Cr}^{3+}$  ions occupy a pyrochlore sublattice with competing nearest-neighbor antiferromagnetic exchange interactions; computational details are given in Table I. The SLD trajectory is annealed from 50 K to 5 K over 5 ps, starting from the ideal cubic structure with random magnetic moments. During the anneal the simulation captures a spontaneous symmetry lowering: the lattice relaxes into an approximately tetragonal structure with  $c < \sqrt{2}a$ , accompanying the establishment of collinear antiferromagnetic order with propagation vector  $\mathbf{q} = (0, 0, 0)$  [Fig. 2(e,f)]. Both the structural distortion and the magnetic ground state are consistent with the spin-driven Jahn–Teller transition to the  $I4_1/amd$  phase predicted by Xiang et al. [40] and observed experimentally below 12.5 K [41], demonstrating that the present framework can capture phenomena in which spin and lattice order emerge cooperatively.

Taken together, these four systems—spanning a two-dimensional magnetic insulator, an itinerant  $3d$  metal, a correlated  $5d$  oxide, and a geometrically frustrated spinel—demonstrate that the present *ab initio* SLD framework can reproduce qualitatively distinct magnetic ground states, including collinear ferromagnetic, non-collinear all-in-all-out, and antiferromagnetic orders, without material-specific parameter adjustments. In all cases, the simulations were initialized from fully random spin configurations and required no prior assumption about the symmetry or type of the target magnetic order, confirming the predictive, rather than postdictive, character of the method. Moreover, the spontaneous tetragonal distortion accompanying magnetic ordering in  $\text{MgCr}_2\text{O}_4$  exemplifies a class of phenomena where the

spin and lattice degrees of freedom are fundamentally coupled; such behavior cannot be captured by atomistic spin-dynamics simulations in which the lattice is frozen, highlighting the need for a coupled SLD treatment.

TABLE I. Computational parameters for the four validation systems.

	$\text{CrI}_3$	bcc Fe	$\text{Cd}_2\text{Os}_2\text{O}_7$	$\text{MgCr}_2\text{O}_4$
Supercell	$2 \times 2 \times 1$	$2 \times 2 \times 2$	conv. cell	conv. cell
Atoms	72	16	40	56
$k$ -mesh	$2 \times 2 \times 1$	$4 \times 4 \times 4$	$2 \times 2 \times 2$	$3 \times 3 \times 3$
Cutoff (eV)	500	500	500	500
$T$ (K)	1	300	1	50→5
$\Delta t$ (fs)	1	0.2	0.5	0.5
Duration (ps)	2	0.4	1	5
$\alpha$	0.2	0.2	0.2	0.2

#### IV. TRAINING-DATA BENCHMARK FOR SLD-ORIENTED SPINGNN MODELS

For spin-aware machine-learning models, training-data construction is nontrivial because the relevant configuration space spans both atomic and magnetic degrees of freedom. A common reference strategy is to combine structural snapshots with independently randomized magnetic configurations. Using SpinGNN [42], a spin-aware graph neural network model, as a concrete test case, we compare models trained on randomized-spin reference data with models trained on data generated from first-principles SLD trajectories. To make this comparison interpretable, we distinguish between the effects of training distribution, training-set size, wall-time budget, and temporal correlation in trajectory-derived data.

For this benchmark, both training datasets are constructed from the same pool of 600 initial atomic structures of an 80-atom  $\text{BiFeO}_3$  supercell with 16 Fe sites carrying local moments. These structures were sampled at equal intervals from a single  $NpT$  molecular-dynamics trajectory generated with the VASP machine-learning force field (MLFF) across 300–900 K. For the reference dataset, each initial structure is combined with 10 fully randomized spin configurations on the Fe sites, following the fully randomized-spin strategy of Ref. [42]. Each resulting spin-lattice configuration is then evaluated by a separate static constrained-moment DFT calculation. For the SLD-derived dataset, each initial structure is used to initialize a 20-step first-principles SLD trajectory, and the 20 trajectory snapshots are used as SLD-derived data points. The two datasets therefore share the same pool of initial atomic structures but differ in how the spin configurations are generated: fully randomized in the reference case and co-evolved with the lattice along SLD trajectories in the SLD-derived case. To avoid information leakage from correlations among data derived from the

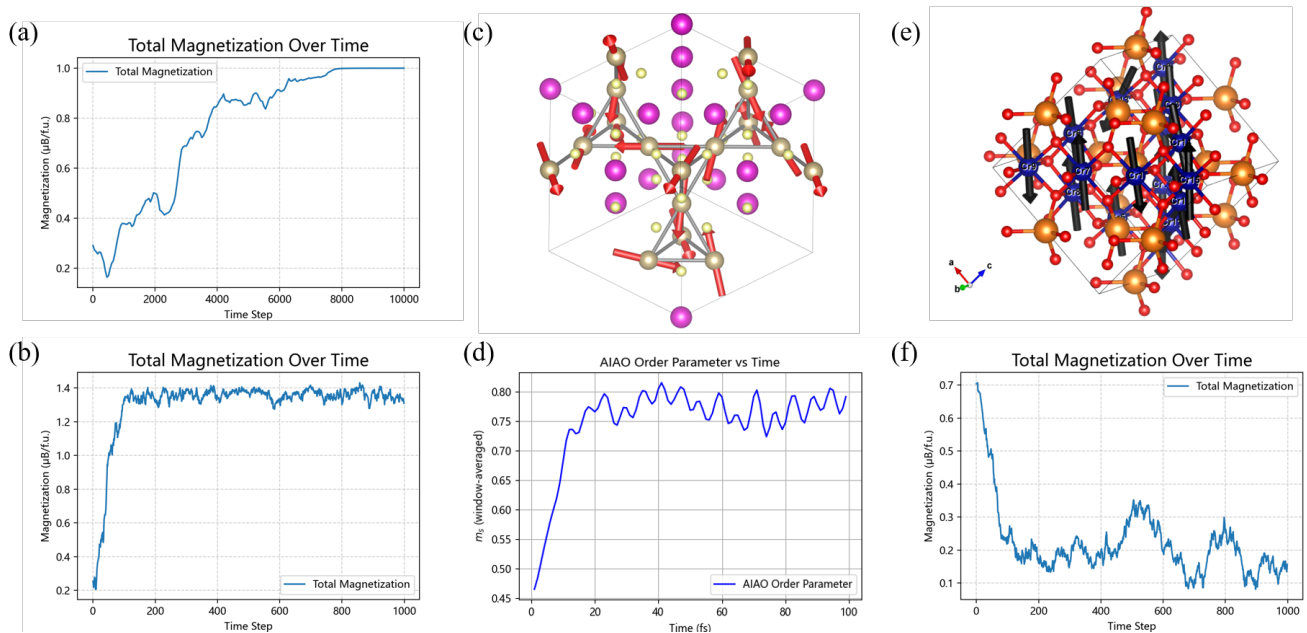


FIG. 2. Magnetic ground-state validation across four representative systems. (a) Monolayer  $\text{CrI}_3$ : convergence of the out-of-plane magnetization from a random initial state to the ferromagnetic ground state. (b) Bcc Fe: convergence of the total magnetization to the collinear ferromagnetic state at 300 K. (c)  $\text{Cd}_2\text{Os}_2\text{O}_7$ : final spin configuration showing the AIAO arrangement. (d)  $\text{Cd}_2\text{Os}_2\text{O}_7$ : time evolution of the AIAO order parameter  $m_s$  converging to  $\approx 0.9$ . (e)  $\text{MgCr}_2\text{O}_4$ : spontaneous tetragonal distortion ( $c/a$  ratio) accompanying the onset of collinear antiferromagnetic order during annealing from 50 K to 5 K. (f)  $\text{MgCr}_2\text{O}_4$ : final spin configuration.

same initial structure, the training and validation sets are split at the level of initial structures rather than individual data points. Because the intended application is subsequent SLD simulation, model performance is evaluated on an independent SLD trajectory that is excluded from both the training and validation sets.

We benchmark models trained on SLD-derived data against those trained on the randomized-spin reference dataset under three comparison protocols. In the first, the SLD-derived and reference models are trained on datasets containing exactly the same number of spin-lattice configurations. In the second, the two models are trained on datasets generated under the same wall-time budget, so they are compared at equal data-generation cost rather than at a fixed number of training configurations. Under the computational settings used here, generating one configuration for the randomized-spin reference dataset requires approximately the same wall time as generating two SLD trajectory snapshots. This cost difference arises because consecutive SLD configurations are close in phase space, so each electronic step can be initialized from the converged state of the preceding one and typically requires fewer SCF iterations than an independently initialized static reference calculation. In the third protocol, we subsample the fixed-wall-time SLD dataset to match the number of training configurations in the reference dataset. This allows us to reduce temporal redundancy and assess the impact of correlations between adjacent trajectory snapshots.

Figures 3(a)–3(c) summarize the benchmark results under the fixed-count protocol. At fixed training-set size, the models trained on SLD-derived data yield prediction errors on the independent SLD test trajectory that are comparable for forces, yet reduced by approximately one order of magnitude for energy and spin forces, relative to the randomized-spin reference models. This suggests that the SLD-derived data provide a training distribution that is better aligned with the independent SLD test trajectory, in the sense that it yields lower prediction errors at the same training-set size.

Under a fixed wall-time budget, the models trained on SLD-derived data show lower MAEs than the randomized-spin reference models on the independent SLD test trajectory. Combined with the fixed-count results, this shows that the stronger performance of the SLD-derived models at equal wall-time arises from two factors: a more effective training distribution and a larger number of training configurations generated within the same computational budget. When the fixed-wall-time SLD dataset is subsampled to reduce temporal correlations at approximately matched training-set size, the resulting models achieve the lowest MAEs across all three protocols, consistent with reduced overfitting to redundant sequential configurations. Taken together, this benchmark demonstrates that dynamically co-evolved spin-lattice trajectories naturally provide a highly effective training distribution for downstream SLD applications, as they directly sample the coupled phase space

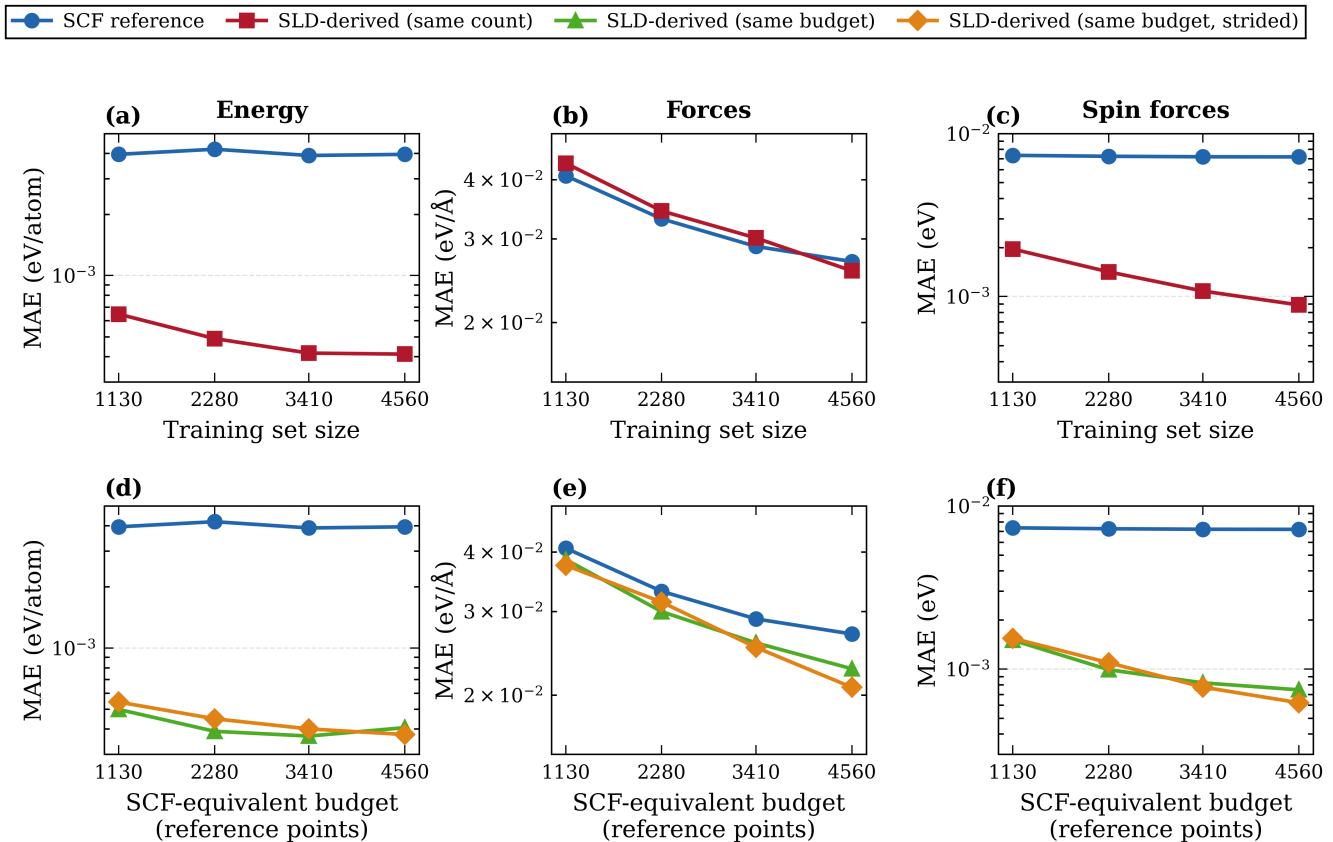


FIG. 3. Training-data benchmark for SLD-oriented SpinGNN models in BiFeO<sub>3</sub>. All mean absolute errors are evaluated on an independent SLD test trajectory. Panels (a)–(c) show the fixed-count comparison between the SCF reference and SLD-derived datasets for energy, forces, and spin forces, respectively. Panels (d)–(f) show the fixed-budget comparison among the SCF reference, the SLD-derived dataset generated at the same SCF-equivalent budget, and its strided counterpart used to reduce temporal correlation. The horizontal axis in the top row is the training-set size, whereas that in the bottom row is the SCF-equivalent data-generation budget, expressed in units of reference SCF-point cost. One SCF reference point requires approximately the same wall time as two saved SLD snapshots.

explored during such dynamics.

## V. DISCUSSION AND CONCLUSIONS

The *ab initio* SLD framework presented in this work circumvents the reliance on pre-fitted exchange interaction parameters typically required in atomistic spin-dynamics simulations [12–14]. By evaluating interatomic forces and effective magnetic fields directly from constrained-moment DFT at each time step, the method enables the simultaneous and mutually consistent evolution of both spin and lattice degrees of freedom. Furthermore, while recent developments suggest that site-specific penalty parameters can further refine constraint accuracy [29], our tests confirm that a global  $\lambda$  is sufficient for the dynamics targeted here; the resulting trajectories remain highly insensitive to its exact magnitude (see Supplemental Material). The validation across four structurally and electronically distinct systems—

encompassing ferromagnetic, non-collinear, and geometrically frustrated magnetic orders—demonstrates that no *ad hoc* parameter adjustments are required to reliably recover these diverse ground states from random initial conditions. The underlying approximations of spin adiabaticity and atomic-moment locality restrict applicability to systems where longitudinal electronic relaxation is sufficiently fast to justify treating moment magnitudes as instantaneously adapting rather than independent dynamical variables. This condition is well satisfied by a broad class of local-moment magnets and by itinerant systems that still sustain well-defined local moments over the time scales of interest, such as bcc Fe, but may break down in weak itinerant magnets or mixed-valence systems where longitudinal fluctuations of the moment magnitude are no longer negligible relative to the orientational dynamics [43, 44]. Within this regime, while the Gilbert damping parameter  $\alpha$  must be assigned a physically realistic value for finite-temperature dynamical studies, it serves merely to control the relaxation time scale when search-

ing for the ground state, leaving the converged magnetic order unaffected as confirmed by our tests.

Beyond its utility for direct physical simulations, the BiFeO<sub>3</sub> benchmark demonstrates that the generated SLD trajectories can serve as an effective source of training data for spin-aware machine-learning potentials, particularly when the downstream task is itself a spin-lattice dynamical simulation. We emphasize, however, that this conclusion does not establish SLD-derived data as universally superior to all possible magnetic-data generation strategies, nor does it imply that randomized magnetic configurations are always an inappropriate baseline. Rather, it demonstrates that for the present SpinGNN model and test protocol, SLD-derived data provide a training distribution that is more representative of the configurations actually encountered during independent SLD simulations than a baseline constructed from identical structural snapshots with randomized spins. Furthermore, the matched-count and strided-sampling comparisons confirm that the temporal correlation inherent to trajectory data does not outweigh this advantage.

The physical origin of this distributional advantage lies in the fact that SLD sampling naturally preserves the dynamic coupling between lattice distortions and magnetic order, thereby avoiding the generation of statistically improbable, high-energy configurations. As either the simulated supercell size or the complexity of its magnetic degrees of freedom increases, uniform random exploration of the high-dimensional spin-configuration space becomes increasingly inefficient, making SLD-based dynamical sampling particularly advantageous for generating training data for spin-aware machine-learning models. This framework also provides a natural route toward active-learning workflows, in which model uncertainty along SLD trajectories triggers new first-principles

calculations in previously undersampled regions.

In summary, the present work establishes a practical fully *ab initio* framework for coupled spin-lattice dynamics in magnetic materials, in which both interatomic forces and effective magnetic fields are obtained self-consistently at each time step from constrained-moment DFT calculations. The successful reproduction of diverse magnetic ground states from random initial conditions demonstrates that this framework is applicable to a broad class of magnets with robust local moments and provides a direct route to finite-temperature simulations of spin-wave and magnon-phonon dynamics as well as magnetostructural transitions. The BiFeO<sub>3</sub>/SpinGNN benchmark further shows that the resulting SLD trajectories can furnish effective training data for spin-aware machine-learning models for downstream spin-lattice simulations. Together, these results establish a direct connection between first-principles spin-lattice dynamics and data-driven modeling of magnetic materials.

#### ACKNOWLEDGMENTS

We acknowledge financial support from the National Key R&D Program of China (Grant No. 2022YFA1402901), the National Natural Science Foundation of China (NSFC, Grant No. 12188101), the Shanghai Science and Technology Program (No. 23JC1400900), the Guangdong Major Project of Basic and Applied Basic Research (Future Functional Materials under Extreme Conditions, Grant No. 2021B0301030005), the Shanghai Pilot Program for Basic Research at Fudan University (No. 23TQ017), the robotic AI-Scientist platform of the Chinese Academy of Sciences, and the New Cornerstone Science Foundation.

- 
- [1] E. Beaurepaire, J.-C. Merle, A. Daunois, and J.-Y. Bigot, *Phys. Rev. Lett.* **76**, 4250 (1996).
  - [2] M. Weißenhofer and P. M. Oppeneer, *Adv. Phys. Res.* **4**, 2300103 (2024).
  - [3] I. V. Solovyev, *Phys. Rev. B* **85**, 054420 (2012).
  - [4] A. Rückriegel, P. Kopietz, D. A. Bozhko, A. A. Serga, and B. Hillebrands, *Phys. Rev. B* **89**, 184413 (2014).
  - [5] K. B. Le, A. Esquembre-Kučukalić, H.-Y. Chen, I. Maliyov, Y. Luo, J.-J. Zhou, D. Sangalli, A. Molina-Sánchez, and M. Bernardi, *Phys. Rev. B* **112**, L180403 (2025).
  - [6] S. A. Wolf, D. D. Awschalom, R. A. Buhrman, J. M. Daughton, S. von Molnár, M. L. Roukes, A. Y. Chtchelkanova, and D. M. Treger, *Science* **294**, 1488 (2001).
  - [7] I. Žutić, J. Fabian, and S. Das Sarma, *Rev. Mod. Phys.* **76**, 323 (2004).
  - [8] A. V. Kimel, A. Kirilyuk, P. A. Usachev, R. V. Pisarev, A. M. Balbashov, and T. Rasing, *Nature* **435**, 655 (2005).
  - [9] C. D. Stanciu, F. Hansteen, A. V. Kimel, A. Kirilyuk, A. Tsukamoto, A. Itoh, and T. Rasing, *Phys. Rev. Lett.* **99**, 047601 (2007).
  - [10] P. Hohenberg and W. Kohn, *Phys. Rev.* **136**, B864 (1964).
  - [11] W. Kohn and L. J. Sham, *Phys. Rev.* **140**, A1133 (1965).
  - [12] V. P. Antropov, M. I. Katsnelson, B. N. Harmon, M. Van Schilfgaarde, and D. Kusnezov, *Phys. Rev. B* **54**, 1019 (1996).
  - [13] B. Skubic, J. Hellsvik, L. Nordström, and O. Eriksson, *J. Phys.: Condens. Matter* **20**, 315203 (2008).
  - [14] R. F. L. Evans, W. J. Fan, P. Chureemart, T. A. Ostler, M. O. A. Ellis, and R. W. Chantrell, *J. Phys.: Condens. Matter* **26**, 103202 (2014).
  - [15] J. Hellsvik, D. Thonig, K. Modin, D. Viñas Boström, A. Bergman, O. Eriksson, L. Bergqvist, and A. Delin, *Phys. Rev. B* **99**, 104302 (2019).
  - [16] I. Stockem, A. Bergman, A. Glensk, T. Hickel, F. Körmann, B. Grabowski, J. Neugebauer, and B. Alling, *Phys. Rev. Lett.* **121**, 125902 (2018).
  - [17] D. Gambino, J. Klarbring, and B. Alling, *Phys. Rev. B* **107**, 014102 (2023).
  - [18] E. Runge and E. K. U. Gross, *Phys. Rev. Lett.* **52**, 997

- (1984).
- [19] C. A. Ullrich, *Time-Dependent Density-Functional Theory: Concepts and Applications* (Oxford University Press, 2012).
- [20] G. Kresse and J. Furthmüller, *Phys. Rev. B* **54**, 11169 (1996).
- [21] G. Kresse and J. Furthmüller, *Comput. Mater. Sci.* **6**, 15 (1996).
- [22] P.-W. Ma and S. L. Dudarev, *Phys. Rev. B* **91**, 054420 (2015).
- [23] J. Behler, *J. Chem. Phys.* **145**, 170901 (2016).
- [24] V. L. Deringer, M. A. Caro, and G. Csányi, *Adv. Mater.* **33**, 2002766 (2021).
- [25] E. V. Podryabinkin and A. V. Shapeev, *Comput. Mater. Sci.* **140**, 171 (2017).
- [26] C. Schran, K. Brezina, and O. Marsalek, *J. Chem. Phys.* **153**, 104105 (2020).
- [27] O. Eriksson, A. Bergman, L. Bergqvist, and J. Hellsvik, *Atomistic Spin Dynamics: Foundations and Applications* (Oxford University Press, 2017).
- [28] M. A. Brännvall, B. Alling, and R. Armiento, *Phys. Rev. B* **113**, 064437 (2026).
- [29] Z. Cai, K. Wang, Y. Xu, S.-H. Wei, and B. Xu, *Quantum Front.* **2**, 21 (2023).
- [30] W. C. Swope, H. C. Andersen, P. H. Berens, and K. R. Wilson, *J. Chem. Phys.* **76**, 637 (1982).
- [31] J. H. Mentink, M. V. Tretyakov, A. Fasolino, M. I. Katsnelson, and T. Rasing, *J. Phys.: Condens. Matter* **22**, 176001 (2010).
- [32] P. E. Blöchl, *Phys. Rev. B* **50**, 17953 (1994).
- [33] G. Kresse and D. Joubert, *Phys. Rev. B* **59**, 1758 (1999).
- [34] M. Parrinello and A. Rahman, *J. Appl. Phys.* **52**, 7182 (1981).
- [35] J. P. Perdew, K. Burke, and M. Ernzerhof, *Phys. Rev. Lett.* **77**, 3865 (1996).
- [36] B. Huang, G. Clark, E. Navarro-Moratalla, D. R. Klein, R. Cheng, K. L. Seyler, D. Zhong, E. Schmidgall, M. A. McGuire, D. H. Cobden, W. Yao, D. Xiao, P. Jarillo-Herrero, and X. Xu, *Nature* **546**, 270 (2017).
- [37] H. Shinaoka, T. Miyake, and S. Ishibashi, *Phys. Rev. Lett.* **108**, 247204 (2012).
- [38] J. N. Reimers, *Phys. Rev. B* **45**, 7287 (1992).
- [39] B. H. Zhang, Z. Wang, and R. Q. Wu, *Phys. Rev. B* **104**, 024411 (2021).
- [40] H. J. Xiang, E. J. Kan, S.-H. Wei, M.-H. Whangbo, and X. G. Gong, *Phys. Rev. B* **84**, 224429 (2011).
- [41] T. Chatterji, G. J. McIntyre, and P.-A. Lindgård, *Phys. Rev. B* **79**, 172403 (2009).
- [42] H. Yu, Y. Zhong, L. Hong, C. Xu, W. Ren, X. Gong, and H. Xiang, *Phys. Rev. B* **109**, 144426 (2024).
- [43] A. V. Ruban, S. Khmelevskiy, P. Mohn, and B. Johansson, *Phys. Rev. B* **75**, 054402 (2007).
- [44] G. M. Stocks, W. A. Shelton, T. C. Schulthess, B. Üjfalussy, W. H. Butler, and A. Canning, *J. Appl. Phys.* **83**, 6509 (1998).